Advances in Water Resources 205 (2025) 105072

Contents lists available at ScienceDirect

Advances in Water Resources

journal homepage: www.elsevier.com/locate/advwatres

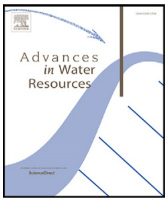

Estimating horizontal velocity in shallow aquifers from temperature perturbations in observation boreholes responding to pumping

Davide Furlanetto

Department of Civil, Environmental and Architectural Engineering, University of Padova, Via Marzolo 9, Padova, 35131, Italy

ARTICLE INFO

Keywords:
Unconfined aquifers
Groundwater temperature
Groundwater velocity
Global sensitivity analysis
In-well techniques

ABSTRACT

The practice of measuring groundwater temperature is growing rapidly and has already demonstrated to be a valuable source of information for estimating soil hydraulic parameters, groundwater–surface water exchanges, and for identifying preferential flow in both fractured and sedimentary aquifers. In the zone of seasonal thermal dynamics of unconfined sedimentary aquifers, temperature measurements in observation wells are found to exhibit a particular perturbation when the water column responds to pumping wells located in the proximity. This paper presents a description of the mechanism underlying this thermal perturbation, validating it by means of three-dimensional numerical modeling, and explores its potential as a source of information. In particular, it presents a framework enabling to estimate in-well water horizontal velocities from the time required for these temperature perturbations to reach a peak. The proposed technique is based on simple data post-processing and does not require additional experimental endeavors beyond the deployment of temperature and pressure sensors. Furthermore, through a global sensitivity analysis based on Monte Carlo numerical simulations, we show that in-well heat propagation begins to show sensitivity to the thermal properties of the well screen, the filter pack and the natural porous medium at thermal Peclet numbers lower than approximately 3.7.

1. Introduction

The quantification of groundwater velocities at the local scale is crucial to accurately address contamination issues and design effective remediation strategies. Methods based on hydraulic head measurements usually provide estimates of spatially averaged flow rates that are informative at the large scale. To measure groundwater flow rates at smaller scales, several tracer-based techniques have been developed over the past decades. Many of these methods involve injecting a solute tracer into a borehole and measuring its concentration over time in the same or a nearby borehole as it migrates under the action of ambient groundwater flow (Devlin, 2020).

Beyond solute tracers, heat has also been widely employed to characterize subsurface flows (Anderson, 2005; Saar, 2011; Rau et al., 2014; Kurylyk et al., 2019). In particular, Fiber Optics Distributed Temperature Sensing (FO-DTS) has recently undergone significant development, enabling the transition from a pointwise spatial scale of investigation to spatially distributed information at high spatial resolution (Selker et al., 2006; Leaf et al., 2012; Bense et al., 2016).

In shallow unconsolidated aquifers, the influence of seasonal atmospheric temperature variations and recharge dynamics typically results in a non-homogeneous vertical temperature profile (Stallman, 1965; Kurylyk et al., 2019), at least during certain times of the year. The zone of seasonal thermal regime is limited to the very shallow subsurface, usually at depths < 20 m, while the geothermal gradient dominates at larger depths (Bense et al., 2016). In the seasonal zone, the analysis of temperature profiles and time series has been widely used to estimate vertical groundwater flow rates, particularly in the vicinity of surface water bodies (Suzuki, 1960; Stallman, 1965; Taniguchi, 1993; Bense and Kooi, 2004; Stonestrom and Constantz, 2003; Holzbecher, 2005; Constantz, 2008; Luce et al., 2013; Rau et al., 2014; Kurylyk et al., 2015). Fewer studies have attempted to use data from naturally occurring temperatures in the shallow subsurface to estimate horizontal flow rates, usually by informing parameter estimation in numerical (Bravo et al., 2002; Su et al., 2004; Xie and Batlle-Aguilar, 2017; Furlanetto et al., 2024) or analytical (Chen et al., 2024) models.

Groundwater temperature data are usually collected by deploying probes or fiber optic cables within monitoring wells (Kurylyk et al., 2019). It has long been recognized that the presence of a borehole, either cased or uncased, induces a distortion of the ambient groundwater flow field (Drost et al., 1968; Sano, 1983; Kearl, 1997; Klammler et al., 2007; Verreydt et al., 2015). The horizontal flow rate through a (vertical) monitoring well $\bar{u}$ $[L\tau^{-1}]$ can be expressed as $\bar{u} = \alpha_D q_\infty$, where q_∞ $[L\tau^{-1}]$ is the undisturbed Darcy flow rate (i.e. in the absence of the well) and α_D $[-]$ is a factor accounting for the distortion of the flow field. Drost et al. (1968) provided an analytic expression for the

---

E-mail address: davide.furlanetto.3@phd.unipd.it.

https://doi.org/10.1016/j.advwatres.2025.105072
Received 30 June 2025; Received in revised form 30 July 2025; Accepted 3 August 2025

distortion factor α_D, here reported in Appendix A, which also considers the influence of a filter pack and a well screen. The effect of the screen slots was investigated numerically by Bayer-Raich et al. (2019). In the absence of a screen and filter pack, an analytic solution for the entire flow field was derived by Sano (1983) and Raja Sekhar and Sano (2000). Therefore, specific corrections are necessary when estimating undisturbed Darcy flow rates from in-well measurements.

Moreover, in the vicinity of drinking water extraction wells, monitoring wells exhibit a hydraulic response to pumping, the latter being an established topic in hydrogeology (de Marsily, 1986; Bear, 1988). In such settings, thermal tracing methods become particularly advantageous, as the release of solute tracers may affect the quality of the extracted water or, at the very least, raise concerns of the water utility companies or the local authorities (Bakx et al., 2023).

To the author's knowledge, little effort has been made to understand the behavior of the temperature profile within a monitoring well under the influence of nearby pumping. In particular, due to relatively high vertical temperature gradients characterizing the seasonal zone, significant temperature perturbations could be induced at shallow depths. In addition, if the monitoring well is screened, horizontal groundwater fluxes could interact, further altering the temperature profile.

This study focuses on very shallow sedimentary formations with large vertical temperature gradients, typical of the zone of seasonal thermal regime. It has three main objectives: the first objective is to investigate the dynamics of the temperature field within a screened monitoring well while it responds to the activation and deactivation of a nearby extraction well; the second objective is to explore the use of in-well temperature perturbations induced by nearby pumping to estimate horizontal flow through the monitoring well; the third objective is to quantify the sensitivity of in-well temperature variations arising from this process to the thermal and hydraulic properties of the well screen, the filter pack and the natural porous medium.

In Section 2.1, we provide a qualitative description of the in-well temperature field under such conditions. Section 2.2 presents the setup of a three-dimensional (3D) finite element model used to reproduce the physical processes. In Section 2.3 we provide a mathematical description of the mechanism and propose a methodology to estimate in-well water horizontal velocities from the analysis of temperature signals. Next, we present the setup of a simplified two-dimensional (2D) horizontal numerical model used to perform a global sensitivity analysis (Section 2.4) on the fluid flow and heat transport parameters via Monte Carlo simulations. In this way, we explore the limitations of the use of thermal tracing methods to estimate in-well water velocities. The results are illustrated and discussed in Section 3, while conclusions are summarized in Section 5.

2. Materials and methods

2.1. Process formalization

Let us consider the following setting, schematized in Figs. 1(a)–(b): in a shallow unconfined sedimentary aquifer, a cased observation well, screened along a portion of its depth and surrounded by a filter pack, is located in the proximity of a pumping well that is activated intermittently (e.g. for water abstraction purposes or during a cross-borehole pumping test). Let us assume that the water column (w), the well screen (s), the filter pack (f) and the natural porous medium (pm) are initially and locally in thermal equilibrium, so that $T_w(z,t_0) = T_s(z,t_0) = T_f(z,t_0) = T_{pm}(z,t_0)$, where T is the temperature $[\theta]$, z is the vertical coordinate $[L]$ and t_0 is a time $[\tau]$. Within the screened interval of the observation borehole, an in-well virtual probe located at z_p (Fig. 1(b)) provides signals of temperature and pressure, namely $T_w(z_p,t)$ and $p_w(z_p,t)$, respectively.

When pumping is activated at time $t = t_0$, a drawdown $s_0(t) > 0$ begins to be observed as the water column within the borehole open space moves vertically (Fig. 2(a), blue line). The probe, which remains in its same position, will begin to record the temperature that at previous times was above z_p (Fig. 2(b)). Therefore, a perturbation of the temperature signal will begin to be observed (Fig. 2(a)). The behavior of the temperature signal at $t > t_0$ would depend on the thermal gradient along the borehole vertical profile in the proximity of z_p. If the in-well temperature is monotonically decreasing with depth above z_p, the temperature recorded at z_p will rise, producing a positive fluctuation $(T_w(z_p,t) - T_w(z_p,t_0) > 0)$ as the one schematized in Fig. 2(a). Naturally, if no vertical gradient of the temperature profile is present close to z_p, as it may occur during some periods of the year (Stallman, 1965; Kurylyk et al., 2019), no temperature perturbation would be observed.

At the same time, drawdown in the surroundings of the observation well will induce a temperature perturbation at z_p in the natural porous medium and in the borehole filter pack, but due to the immobility and specific heat capacity of the solid matrix, the temperature reached in the porous media will differ from the one in the observation well at the same depth, and will likely be almost unchanged. This will induce a temperature gradient between the water column within the monitoring well and the surrounding porous media. Therefore, lateral heat transfer will tend to dissipate the water temperature perturbation in the well open space, ultimately leading to $T_w(z_p,t) \rightarrow T_{pm}(z_p,t)$, hence a new thermal equilibrium condition (Fig. 2(a)). This would induce a peak of the temperature perturbation at time $t = t^\star$. A schematic representation of the temperature profile within the monitoring well at $t = t_0$ and $t = t^\star$ is offered in Fig. 1(c). The probe being located in a screened portion of the observation well, both thermal advection and conduction concur to the latter dissipation process. If the dissipation of the thermal perturbation occurring between t_0 and $t^\star$ is advection-dominated, it would be potentially possible to establish a relationship between the time required for the temperature signal to reach the peak and the in-well water horizontal velocity established between t_0 and $t^\star$. A comparison with a temperature probe located in a non-screened portion of the observation well could allow to evaluate experimentally whether heat transport is dominated by advection or conduction.

When pumping is deactivated at time t_1, a counter-fluctuation would be observed in the temperature signal due to vertical upward velocities in the water column. Due to the same mechanism illustrated above, temperature will again experience an initial perturbation that is dissipated in time due to lateral heat transfer. If the temperature profile close to z_p is monotonic, the temperature perturbation observed after pumping deactivation would be opposite with respect to the one occurring during pumping, as illustrated in Fig. 2(a).

The process described above was observed experimentally, and illustrative data are reported in the Supplementary Information. In this study, however, it was reproduced and interpreted via a complete 3D finite element numerical model coupling flow and heat transport. Moreover, we propose a more computationally efficient quasi-2D semi-analytical approach to model this temperature dynamics.

2.2. Complete 3D numerical model

A complete 3D finite element model was set up in COMSOL Multiphysics® v. 5.2 (2016) to investigate the flow field and the heat transport transient dynamics in an observation well responding to a nearby pumping well, with the purpose of validating the mechanism illustrated in the previous Section 2.1.

The 3D model domain is contextualized within the setting of this study as delineated by the dashed lines in Figs. 1(a)–(b). A 4-inch diameter polyvinyl chloride (PVC) pipe (51.6 mm inner radius, 57.0 mm outer radius) is located at the center of a 2.5 m high prismatic domain, having a 0.8 m wide and 1.0 m long rectangular base. The pipe is encircled by a 1-inch thick filter pack. Four distinct material compartments are considered: water (within the observation well), the (perforated) PVC material of the well screen, the porous filter pack and the natural porous medium. Following Drost et al. (1968), the well screen is

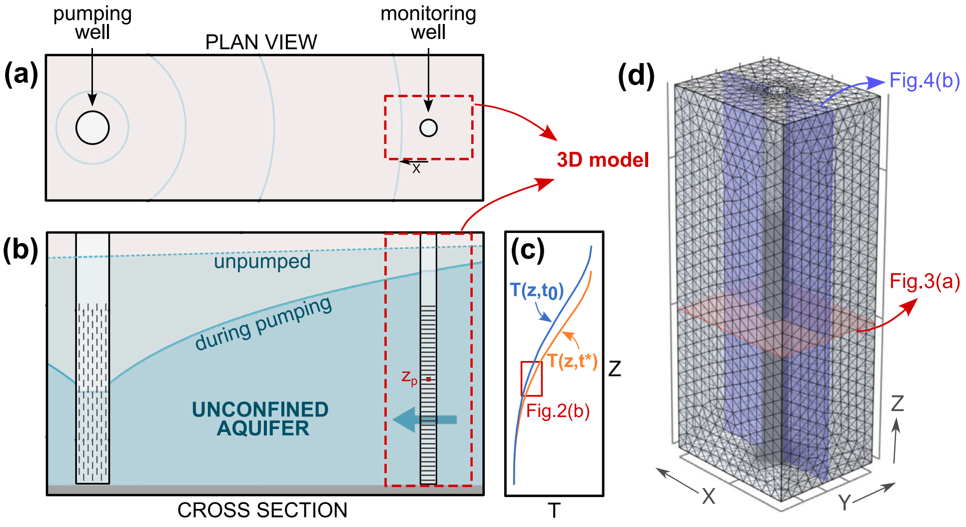

Fig. 1. Schematic (a) plan view and (b) cross section of the setting of the present study. In a shallow unconfined sedimentary aquifer, a monitoring well responds to the activation of a pumping well located nearby. Note that the scheme is not in scale. (c) Schematic behavior of the temperature profile within the monitoring well in response to pumping. (d) Mesh of the complete 3D model and position of the horizontal cross section depicted in Fig. 3 and the vertical cross section in Fig. 4(b).

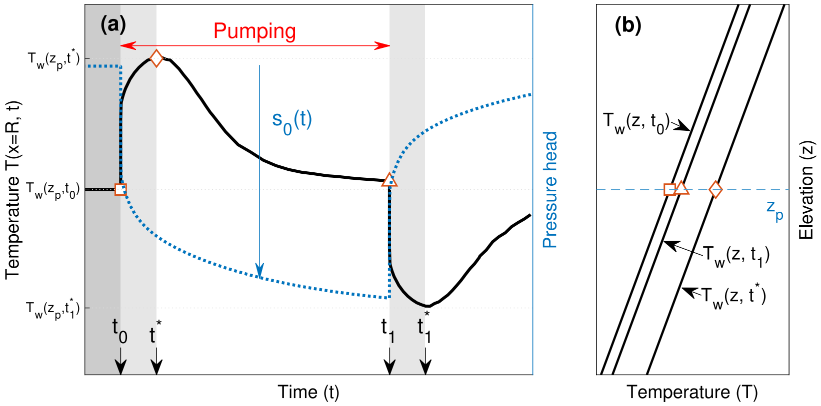

Fig. 2. (a) Schematic behavior of temperature (black) and pressure head (blue) in time at the center of the observation well responding to a pumping well, at a fixed depth z_p. (b) Schematic behavior of the temperature vertical profile within the monitoring well in the vicinity of z_p. The temperature profile is assumed linear for descriptive purposes. The three different markers indicate corresponding temperatures in panels (a) and (b) at three representative times.

simulated as an equivalent porous medium. The model parameters are assumed to be homogeneous within each material compartment. The well screen and the filter pack are limited to the lower 1.7 m deep portion of the domain, while in the upper 0.8 m the well is considered to be cased and grouted (hence hydraulically isolated from the aquifer material). The 3D model mesh is shown in Fig. 1(d). A horizontal cross section of the domain across the screened portion of the piezometer is schematized in Fig. 3. A vertical cross section passing through the center of the monitoring well is schematized in Fig. 4(b).

In the water column contained within the well, the Navier–Stokes equations are solved by assuming the inertial terms are negligible (Stokes flow) and the fluid is incompressible, leading to

$$\rho_w \frac{\partial \mathbf{u}}{\partial t} = \nabla \cdot [-p_w \mathbf{I} + \mu(\nabla \mathbf{u} + (\nabla \mathbf{u})^T)] + \rho_w \mathbf{g} \tag{1}$$

$$\rho_w \nabla \cdot \mathbf{u} = 0 \tag{2}$$

where ρ_w is the water density $[ML^{-3}]$, $\mathbf{u}$ is the velocity vector $[L\tau^{-1}]$, t is time $[\tau]$, p_w is the water pressure $[ML^{-1}\tau^{-2}]$, $\mathbf{I}$ is the identity tensor, μ is the water dynamic viscosity $[ML^{-1}\tau^{-1}]$ and $\mathbf{g}$ is the acceleration of gravity vector$[L\tau^{-2}]$.

The upper portion of the water column is simulated via a moving mesh, imposing an external pressure equal to zero (i.e. atmospheric pressure) on its upper boundary (Fig. 4(b)). A moving mesh approach enables dynamic adjustments of the domain geometry in response to the simulated physical processes. This allows for simulating the displacement of the water column induced by the water table drawdown, which is in turn caused by the activation of a hypothetical pumping well in the proximity.

Richards' equation is resolved in the natural porous medium, in the filter pack and in the well screen

$$\nabla \cdot \left[\frac{k_{sat} k_r}{\mu} (\nabla p + \rho_w \mathbf{g}) \right] = \left(S_e S + \frac{C_m}{\rho_w g} \right) \frac{\partial p}{\partial t} \tag{3}$$

where p $[ML^{-1}\tau^{-2}]$ is the pore water pressure, k_{sat} is the saturated permeability $[L^2]$, k_r $[-]$ is the relative permeability, S_e $[-]$ is the effective saturation, S $[M^{-1}L\tau^2]$ is the storage coefficient and C_m is the specific moisture capacity $[L^{-1}]$. Relative permeability k_r, effective saturation S_e, and specific moisture capacity C_m have been defined according to van Genuchten model (Van Genuchten, 1980). Ambient groundwater flow is induced by a 0.1% hydraulic head gradient, obtained by imposing Dirichlet boundary conditions on two opposite sides of the soil column (see Fig. 3(a)). The hydraulic head time series imposed as boundary conditions are shown in Fig. 4(a): after a 14 min model warm-up period with static water levels, which ensured steady hydraulic conditions, hydraulic head decreases as if it were

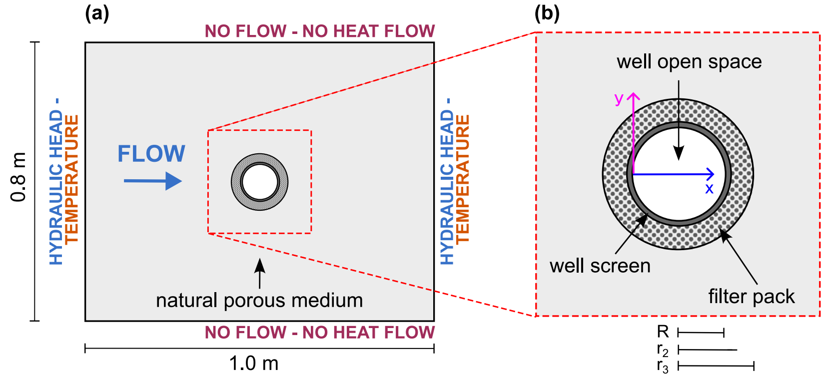

Fig. 3. Schematic of a horizontal cross section of the 3D model along the screened portion of the monitoring well as indicated in Fig. 1(d). (a) Complete section: the mean groundwater flow direction is indicated with the blue arrow and the model's external boundary conditions are indicated on the four sides. (b) Close-up view in the proximity of borehole, with indication of the different material compartments.

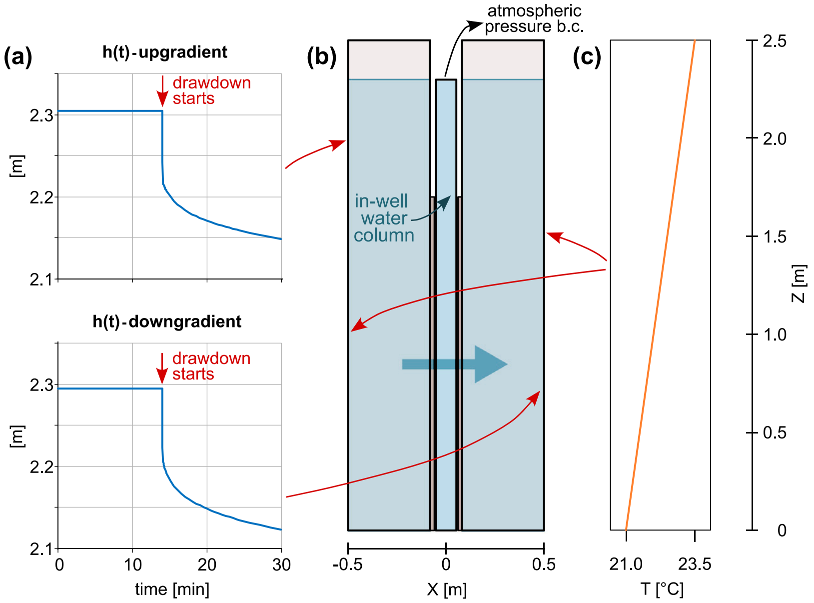

Fig. 4. Boundary conditions of the 3D model. (a) Hydraulic head time series imposed as boundary conditions on the two indicated sides of the domain. (b) Schematic of a vertical cross section of the 3D model domain passing through the center of the monitoring well, as indicated in Fig. 1(d). (c) Temperature profile imposed as boundary condition on the two indicated sides of the domain, and as initial condition.

responding to the activation of a pumping well. The pumping-forced water table drawdown is simulated by imposing transient hydraulic head obtained from Neuman's analytic solution (Neuman, 1972). The simulated period is 30 min. Slight deviations of the hydraulic gradient from the ambient 0.1% occur during the initial phase of drawdown. A no-flow condition is imposed on all the other boundaries.

The two flow equations – Stokes' in the free fluid and Richards' in the porous media – are coupled at the inner interface between the well screen and the well open space, hereafter named Γ, by imposing continuity of mass (4) and continuity of the normal stresses (5), namely (Jones, 1973; Arbogast and Brunson, 2007):

$$\mathbf{q} \cdot \mathbf{n} = \mathbf{u} \cdot \mathbf{n} \quad \text{on } \Gamma \tag{4}$$

where $\mathbf{q}$ is Darcy's flux $[L\tau^{-1}]$ in the well screen, $\mathbf{u}$ is the water velocity in the borehole space $[L\tau^{-1}]$ and $\mathbf{n}$ is the normal to the Γ surface, and

$$\mathbf{n}^T \cdot (-p_w \mathbf{I} + \mu(\nabla \mathbf{u} + (\nabla \mathbf{u})^T))\mathbf{n} = -p_s \quad \text{on } \Gamma \tag{5}$$

where p_w $[ML^{-1}\tau^{-2}]$ is the pressure of free water (i.e. in the borehole space), p_s $[ML^{-1}\tau^{-2}]$ is the water pressure in the well screen, $\mathbf{I}$ is the identity matrix and μ is the water dynamic viscosity $[ML^{-1}\tau^{-1}]$.

Flow through the well screen is assumed to be radial, consistently with a flow-converging effect of the screen slots. Hence, an anisotropic hydraulic conductivity tensor is assigned to the well screen domain and only normal flow is allowed at the Γ interface, namely

$$\mathbf{u} \cdot \mathbf{t} = 0 \quad \text{on } \Gamma \tag{6}$$

where $\mathbf{t}$ is the tangent vector to Γ. The permeabilities of the other material compartments are assumed isotropic.

Heat transport equations are solved both in the free fluid and in the porous media. The heat transport equation in free water is

$$\rho_w C_{p,w} \frac{\partial T}{\partial t} + \rho_w C_{p,w} \nabla \cdot (\mathbf{u}T) = \nabla \cdot (\lambda_w \nabla T) \tag{7}$$

where $C_{p,w}$ is the specific heat capacity of water at constant pressure $[L^2\tau^{-2}\theta^{-1}]$, T is the temperature $[\theta]$, and λ_w is the thermal conductivity $[L^3\tau^{-3}\theta^{-1}]$ of water. Heat transport in the porous media is simulated, under the hypothesis of local thermal equilibrium (Kaviany, 1995), by resolving the following

$$(\rho C_p)_{pm} \frac{\partial T}{\partial t} + \rho_w C_{p,w} \nabla \cdot (\mathbf{u}T) = \nabla \cdot (\lambda_{pm} \nabla T) \tag{8}$$

where $(\rho C_p)_{pm}$ is the volumetric heat capacity $[ML^{-1}\tau^{-2}\theta^{-1}]$ of the bulk porous medium and λ_{pm} $[L^3\tau^{-3}\theta^{-1}]$ is its effective thermal conductivity (neglecting thermal dispersion). These have been computed, for each material compartment, as described in the following Section 2.4.3 by Eqs. (25) and (26).

A vertical temperature gradient of 1 °C/m is imposed as both the initial condition and the boundary conditions on the same lateral sides of the prismatic domain where the hydraulic head is specified, as shown in Figs. 3(a) and 4(c). Since the vertical extent of the domain is limited due to computational constraints, a linear temperature profile is assumed as a local approximation of Stallman's solution (Stallman, 1965). No thermal flux is prescribed on the other two sides (Fig. 3(a)). A constant temperature is imposed on the top and bottom surfaces of the prismatic domain. Thermal coupling at the Γ interface between the well screen and the free fluid is obtained by imposing the same temperature, namely

$$T_w = T_s \quad \text{on } \Gamma \tag{9}$$

which is consistent with the local thermal equilibrium assumption (Kaviany, 1995).

From the computational point of view, the flow and heat transport problems are solved sequentially, the solution of the former informing the latter through the simulated flow field.

2.3. Quasi-2D semi-analytical model

In this section we propose a simplified method to model the temperature dynamics within the open space of a monitoring well (Fig. 3(b)) responding to a nearby pumping well.

We assume here that the dependence on time of the horizontal components of the velocity field within the monitoring well open space is negligible and we define the average velocity $[L\tau^{-1}]$ in the horizontal flow direction (oriented as the x axis in Fig. 3(b)) as

$$U_0^x = \frac{1}{2R}\int_0^{2R} u(x,0)dx \tag{10}$$

We denote as $s_0(t) > 0$ the drawdown $[L]$ in the observation well as a function of time, e.g. as measured by a pressure probe. We assume that the vertical components of the velocity w $[L\tau^{-1}]$ in the water column are homogeneous at any given elevation z (thus assuming a plug flow motion), hence $w = w(z,t)$, and that no buoyancy-related vertical flow occurs. Considering a homogeneous aquifer and a monitoring well with a screened interval of length H $[L]$ with no bottom outflow, and posing $z = 0$ at the lower end of the well, it is possible to show by mass continuity that

$$w(z,t) = -\frac{z}{H}\frac{ds_0(t)}{dt} \tag{11}$$

as long as the free surface does not intersect the well screen. More details on the derivation of Eq. (11) are reported in Appendix B.

Being $w = dz/dt$, Eq. (11) becomes

$$\frac{1}{z}\frac{dz}{dt} = -\frac{1}{H}\frac{ds_0}{dt} \tag{12}$$

and by integrating both sides, assuming $s_0(t_0) = 0$ and denoting the initial elevation of a water particle as $z_0 = z(t_0)$, it yields

$$\ln\left(\frac{z(t)}{z_0}\right) = -\frac{s_0(t)}{H} \tag{13}$$

from which the elevation at time t of a water particle at an initial elevation z_0 follows as

$$z(t) = z_0 \exp\left(-\frac{s_0(t)}{H}\right) \tag{14}$$

In a semi-infinite purely-fluid 1D horizontal domain $x \geq 0$ (at given z), where the center of the borehole open space is located at $x = R$ (Fig. 3(b)), let us consider the 1D advection-diffusion equation in water:

$$\frac{\partial T}{\partial t} + U_0^x\frac{\partial T}{\partial x} = \alpha_w\frac{\partial^2 T}{\partial x^2} \tag{15}$$

where $T = T(x,t)$ and α_w $[L^2\tau^{-1}]$ is the thermal diffusivity of water. Also, the initial $(t = t_0)$ temperature profile will be $T^0(z)$. Moreover, we assume that the temperature of the porous media, at least upgradient, is conserved and equal to the initial temperature profile, so that $T(x = 0,t)|_z = T^0(z)$, and we will rely on the hypothesis of local thermal equilibrium. Then, a virtual probe located at a fixed position z_p would "see" at each time t the 1D temperature field that, considering (14), at time t_0 was located at

$$z_0 = z_p\left(\exp\left(-\frac{s_0(t)}{H}\right)\right)^{-1} \tag{16}$$

having experienced a transient boundary condition

$$g(x=0,t) = T^0\left(z_0\exp\left(-\frac{s_0(t)}{H}\right)\right)$$

Therefore, (15) is subject to the initial and boundary conditions

$$\begin{aligned} T(x,t_0) &= T^0(z_0), \quad t = t_0 \\ T(0,t) &= T^0\left(z_0\exp\left(-\frac{s_0(t)}{H}\right)\right), \quad x = 0 \\ T(x,t) &= T^0(z_0), \quad x \to +\infty \end{aligned} \tag{17}$$

The 1D temperature field at z_p would then be, at each time t, a solution of (15)–(17) obtained for a different z_0, given by (16), thus different initial and boundary conditions. Hence, to obtain $T(R,t)|_{z_p}$, it is sufficient to fully evaluate (15)–(17) (e.g., numerically) at z_0 given by (16) for each time t and extract the solution at $x = R$. Naturally, this approach disregards heat conduction along the vertical, but vertical temperature gradients are usually much lower than the horizontal gradient that is originated by the drawdown.

The initial boundary value problem (15)–(17) can be used to model the temperature field $T(x,t,z)$ in the borehole space of an observation borehole that responds to a drawdown $s_0(t)$. In particular, knowing $s_0(t)$ and the temperature profile in the proximity of a given z_p, the temperature perturbation caused by the drawdown would depend only on the velocity U_0^x, and by fitting the simulated curve to experimental temperature data it is conceptually possible to obtain an estimate of U_0^x. As recalled in the Introduction, by applying to the latter a suitable flow converge factor it would then be possible to obtain an estimate of the horizontal Darcy's flow rate.

The initial temperature profile might be known (e.g., via FO-DTS) with a spatial resolution along z that is usually insufficient to accurately model the actual temperature behavior. However, only the temperature profile in the vicinity of z_p would be significant to model $T(z_p)$ and could, for instance, be approximated linearly. Hence, by capturing the timing of the peak, rather than the temperature at the peak for example, an estimate of U_0^x could be obtained even with poor knowledge of the initial temperature profile.

Note that this model is valid also after pumping deactivation, during the recovery of undisturbed hydraulic conditions. Both estimates of U_0^x, during pumping activation or deactivation, would be representative of an average in-well flow field between the time at which the observation well begins to respond to pumping and the peak time $t^\star$, which might not necessarily be representative of the undisturbed flow conditions.

In any case, posteriorly, it would be necessary to compute a thermal Peclet's number $[-]$

$$Pe_t = \frac{U_0^x R}{\alpha_w} \tag{18}$$

here defined using the radius R of the borehole open space as the characteristic length and the thermal diffusivity of water α_w, in order to assess whether the heat transport process dominated by advection or conduction. This could ensure that the estimated velocity is not significantly affected by the variability in the thermal parameters of the well screen, the filter pack or the natural porous medium, which are usually unknown and the model presented in this Section is not accounting for. The influence of these parameters and a threshold value for the Peclet's number (18) to ensure such a condition are explored in the following sensitivity analysis.

A numerical experiment has been carried out comparing the 3D numerical model of Section 2.2 and the quasi-2D semi-analytical model of this Section, where the latter has been solved via a finite-difference scheme in MATLAB. In particular, synthetic time series of temperature and drawdown are obtained from simulations of the 3D numerical model. The simulated drawdown is used to apply the method proposed in this Section to estimate the in-well average horizontal velocities by fitting the timing of the peak. The latter estimates are then compared to those simulated by the 3D model. These results are described in Section 3.1.1.

An application of the quasi-2D semi-analytical model using experimental data is presented in the Supplementary Information. Although the results are promising, the temporal resolution of the data is not adequate to accurately capture the position of the peak, and the example is therefore intended for illustrative purposes.

2.4. Global sensitivity analysis

To investigate to what extent the analysis of thermal perturbations within a monitoring well open space can be informative of in-well horizontal velocities, we performed a global sensitivity analysis (GSA) using a simplified 2D numerical model set up in COMSOL Multiphysics® v. 5.2 (2016). The aim is to assess under which conditions uncertainty on model parameters may hinder the accurate estimation of in-well horizontal velocities. The GSA is based on the computation of Sobol's and AMA indices, described in Section 2.4.2. The following Section 2.4.1 illustrates the setup of the 2D numerical model.

2.4.1. Horizontal 2D numerical model for the GSA

As described in the previous sections, the temperature field in the open space of the screened observation well, at any given time, would depend on the interplay between the horizontal flow velocity within the well open space and the vertical velocities of the water column induced by the drawdown. Since the 2D horizontal numerical model described here cannot intrinsically reproduce the effect of the drawdown, and in order to homogenize the results of the following sensitivity analysis, here we study the time required to partly dissipate an initially ($t = 0$) homogeneous temperature anomaly within the well open space under steady flow conditions.

The geometry of the 2D model used for the GSA reproduces a horizontal cross section of the 3D model described in Section 2.2 across its (saturated) screened portion (Fig. 1(d)), and corresponds to the scheme in Fig. 3.

The flow in the well open space (Fig. 3(b)) is simulated solving Navier–Stokes equations in steady-state, under the assumption of incompressible flow. The steady-state Navier–Stokes equation is provided by

$$\rho_w(\mathbf{u}\cdot\nabla)\mathbf{u} = \nabla\cdot[-p_w\mathbf{I} + \mu(\nabla\mathbf{u} + (\nabla\mathbf{u})^T)] \tag{19}$$

while the incompressibility condition is provided by (2).

The flow in the porous media (i.e. well screen, filter pack and natural porous medium) is solved via the groundwater flow equation, given by

$$\frac{\partial}{\partial t}(\phi\rho_w) = \nabla\cdot\mathbf{q} \tag{20}$$

$$\mathbf{q} = -\mathbf{k}\nabla p/\mu \tag{21}$$

where ϕ is the porosity [-], $\mathbf{q}$ is Darcy's flow rate $[L\tau^{-1}]$, $\mathbf{k}$ the tensor of saturated intrinsic permeability $[L^2]$ and p the pore water pressure.

Heat transport in the borehole space is simulated by solving Equation (7), whereas heat transport in the porous compartments is simulated via Equation (8). In this case, since the model is 2D, vector variables have two components.

Steady-state flow across the domain is induced by a 0.1% hydraulic head gradient, obtained by imposing Dirichlet boundary conditions on the two opposite sides of the domain indicated in Fig. 3(a). On the same two opposite sides, temperature is prescribed. The remaining two boundaries are assigned no-flow and no-heat-flow conditions (Fig. 3(a)). Flow and thermal coupling conditions at the Γ interface are the same already presented for the 3D model (Eqs. (4) to (9)). The permeability tensor of the well screen is assumed to be anisotropic in order to force flow through the well screen to be radial. The permeability of the other materials is assumed to be isotropic.

The 2D mesh has a total number of 25616 elements and is more refined close to the well open space. The flow and heat transport problems are solved sequentially, the solution of the former informing the latter through the simulated flow field, once steady flow conditions are reached.

A temperature anomaly is simulated by imposing a homogeneous initial temperature T_1 in the borehole open space that is 1 °C higher with respect to the other material compartments, where the initial temperature is T_0. We define a dimensionless recovery factor $\beta(x,t)$ as

$$1 - \beta(\mathbf{x},t) = \frac{T(\mathbf{x},t) - T_0}{T_1 - T_0} \tag{22}$$

so that $0 \le \beta \le 1$, indicating the fraction of initial temperature difference that is recovered at time t at the spatial coordinate $\mathbf{x}$. The time required to recover a fraction β of the initial temperature perturbation will be referred to as t_β. The value $(1-\beta)$ is analogue to the Relative Temperature Anomaly used by Read et al. (2013). In particular, (22) is evaluated at $\mathbf{x} = (R, 0)$, i.e., at the center of the borehole space. Therefore, the recovery time t_β analyzed in the sensitivity analysis is different from the time required to reach a temperature peak, previously indicated with $t^\star$, but is used to assess the influence of the uncertainty in the material properties of the different compartments.

A simplified analytical model reproducing the process that is analyzed in the GSA in a purely-fluid 1D domain is illustrated in Appendix C and the results of the numerical simulations are compared with Eq. (C.2).

2.4.2. Sensitivity indices for the GSA

Given a vector of parameters $\mathbf{p} = (p_1, p_2, \dots, p_k)$, a scalar output of a model f can be indicated as $y = f(\mathbf{p})$. For each parameter p_i, the first-order (or principal) Sobol's index is defined as (Sobol', 2001)

$$S_i = \frac{V_{p_i}\left[E_{\mathbf{p}\sim i}\left[y \mid p_i\right]\right]}{V\left[y\right]} \tag{23}$$

where V is the variance operator and E is the expectation operator. The symbols with subscript $\mathbf{p}\sim i$ remark that the statistical moment is taken while keeping p_i fixed, while those with subscript p_i denote that the statistical moment is taken over all possible values of p_i. The principal Sobol's index is a measure of the first-order effect of p_i on the model output y, and can also be interpreted as the relative expected reduction of variance that would be obtained if p_i could be fixed (Saltelli et al., 2010).

More recently, Dell'Oca et al. (2017) introduced new indices to quantify the impact of the parameters on the first four statistical moments of y, and they have already been employed for GSA in the field of hydrogeology (Bianchi Janetti et al., 2019). In general, for the statistical moment M, the index $AMAM_{p_i}$ is defined as:

$$AMAM_{p_i} = \frac{E_{p_i}\left[\left|\, M\left[y\right] - M_{\mathbf{p}\sim i}\left[y \mid p_i\right] \,\right|\right]}{M\left[y\right]} \tag{24}$$

provided that $M[y] \neq 0$. It can be interpreted as the expected relative variation of the moment M of y due to variations of p_i only (Dell'Oca et al., 2017).

The principal Sobol' index S and the AMA indices for the expected value ($AMAE$), the variance ($AMAV$) and the skewness ($AMA\gamma$) have been computed for the distortion factor α_D, as provided by the analytic

Table 1
Model parameters that are considered uncertain in the global sensitivity analysis. For each parameter, its sample space is defined with a range (lower and upper bound) and a scale.

Compartment	Parameter	Symbol	Unit	Range	Scale
Well screen	Density of PVC	ρ_{g1}	10^3 Kg/m^3	1.33 ÷ 1.65	Linear
	Permeability	k_1	m^2	−12 ÷ −5	Log10
	Porosity	ϕ_1	–	0.03 ÷ 0.2	Linear
	Specific heat	C_{p1}	J/Kg K	$8 \cdot 10^2 \div 1 \cdot 10^3$	Linear
	Thermal conductivity	λ_{s1}	W/m K	0.14 ÷ 0.28	Linear
Filter pack	Density of grains	ρ_{g2}	10^3 Kg/m^3	1.9 ÷ 7	Linear
	Permeability	k_2	m^2	−12 ÷ −7	Log10
	Porosity	ϕ_2	–	0.2 ÷ 0.5	Linear
	Specific heat	C_{p2}	J/Kg K	$4 \cdot 10^2 \div 1 \cdot 10^3$	Linear
	Thermal conductivity	λ_{s2}	W/m K	0.18 ÷ 4.5	Linear
Nat. medium	Density of grains	ρ_{g3}	10^3 Kg/m^3	1.9 ÷ 7	Linear
	Permeability	k_3	m^2	−13 ÷ −7	Log10
	Porosity	ϕ_3	–	0.2 ÷ 0.7	Linear
	Specific heat	C_{p3}	J/Kg K	$4 \cdot 10^2 \div 1 \cdot 10^3$	Linear
	Thermal conductivity	λ_{s3}	W/m K	0.18 ÷ 4.5	Linear

model (A.2) with 10^5 sets of parameters. The principal Sobol' index S, the $AMAE$ and the $AMAV$ have been computed for the time t_β required to recovery 70% of the initially homogeneous temperature anomaly, hereafter named t_{70}, simulated via the 2D horizontal model (Section 2.4.1) run with a total of about $1.1 \cdot 10^4$ parameters sets. We also computed the first- and second-order statistical moments of these variables conditional to each parameter.

The model parameters considered uncertain and their treatment for the purposes of the GSA are described in the following Section 2.4.3.

2.4.3. Parameterization of the 2D horizontal numerical model for the GSA

The physical properties of water are assumed to be known. The physical properties of the well screen, the filter pack, and the natural porous medium, listed in Table 1, are assumed to be uncertain. For each model run, a set of $k = 15$ uncertain parameters is generated by randomly sampling a point in the unit hypercube, and by linearly scaling its coordinates in the corresponding parameter spaces (Table 1). Thus, all parameters are assumed to have a uniform probability density distribution in their space and to be uncorrelated. The range within which each parameter can vary has been selected to represent a wide variety of field conditions. The range values for the density and specific heat capacity at constant pressure of the solid grains were selected from Waples and Waples (2004), while the range values of permeability and porosity were selected from Bear and Cheng (2009). The range values for the thermal conductivity of the solid grains were taken from Anderson (2005). The values for the parameters of the (screened) PVC pipe were taken from typical technical files of producers.

For each different porous material compartment (see Fig. 3), volumetric heat capacities $(\rho C_p)_{pm}$ and effective thermal conductivities λ_{pm} have been computed as (Bear, 1988; Anderson, 2005; Rau et al., 2014):

$$(\rho C_p)_{pm} = \phi(\rho_w C_{p,w}) + (1-\phi)(\rho_g C_{p,g}) \tag{25}$$

$$\lambda_{pm} = \phi\lambda_w + (1-\phi)(\lambda_g) \tag{26}$$

where ρ_g, $C_{p,g}$, and λ_g are the density $[ML^{-3}]$, the specific heat capacity at constant pressure $[L^2\tau^{-2}\theta^{-1}]$, and the thermal conductivity $[L^3\tau^{-3}\theta^{-1}]$, respectively, of the solid grains. These equations have been extended also to the well screen although not properly a granular material. The parameters are considered to be homogeneous within each compartment.

3. Results

3.1. Results of the complete 3D numerical model

Fig. 5(a) depicts the temperature field across a vertical x-z cross-section of the 3D model, passing through the center of the borehole, at three different time steps: before the activation of the pumping well (left), at the maximum temperature peak during the drawdown (center) and during the thermal dissipation phase (right), still during the drawdown. The vertical cross section corresponds to the one schematized in Fig. 4(b) and indicated in Fig. 1(d). Fig. 5(b) shows the temperature field at the same times across a horizontal cross-section located at 1.3 m from the bottom of the model domain. The time series of temperature and drawdown simulated at the center of the well open space in the latter cross-section correspond to those displayed in Fig. 6.

In the initial phase of the drawdown, the vertical velocity in the water column contained in the borehole open space induces a differential perturbation of the temperature field with respect to the outer compartments. The amplitude of the perturbation is smaller close to the bottom of the domain because the vertical velocity in the water column decreases with depth, consistently with (11). Concurrently, lateral heat transfer induces a migration of the latter perturbation in the flow direction (from left to right in Fig. 5), which is responsible for the dissipation of the temperature perturbation within the monitoring well open space.

An analysis of the flow field (details not shown) confirmed that the distortion of the flow field induced by the borehole is well captured by the model and not significantly influenced by the boundary conditions. The 3D model shows minor numerical instability issues for the heat transport problem, but the results appear not to be substantially affected. Overall, the results of the 3D model simulations support the qualitative description of the mechanism presented in Section 2.1.

3.1.1. Demonstrative example of velocity estimation

In this Section we illustrate an example in which we performed the estimation of the in-well water velocity by using the quasi-2D semi-analytical model of Section 2.3.

In the 3D numerical model, the horizontal average velocity U_0^x is slightly varying with time during the drawdown phase, hence the following evaluation is done with respect to the time-averaged value

$$\langle U_0^x \rangle = \frac{1}{t^\star - t_0}\int_{t_0}^{t^\star} U_0^x(t)\,dt \tag{27}$$

The time series of temperature and drawdown of the 3D numerical model at three different depths, together with those of the quasi-2D model at the same depths, are shown in Fig. 6. In particular, using (15)–(17) and by manually adjusting the average in-well horizontal velocity to capture the timing of the peak $t^\star$, we obtain an estimate of $log_{10}[U_0^x] = -3.32$, while the 3D model provides $log_{10}[\langle U_0^x \rangle] = -3.24$. The relative error of the estimate on the (log) average velocity is therefore 2.54%.

From Fig. 6, we can observe that the actual temperature perturbations are different, the ones of the 3D model displaying higher temperatures. The mean absolute errors between the 3D model and the quasi-2D model, computed over the time window from 14 to 20 min,

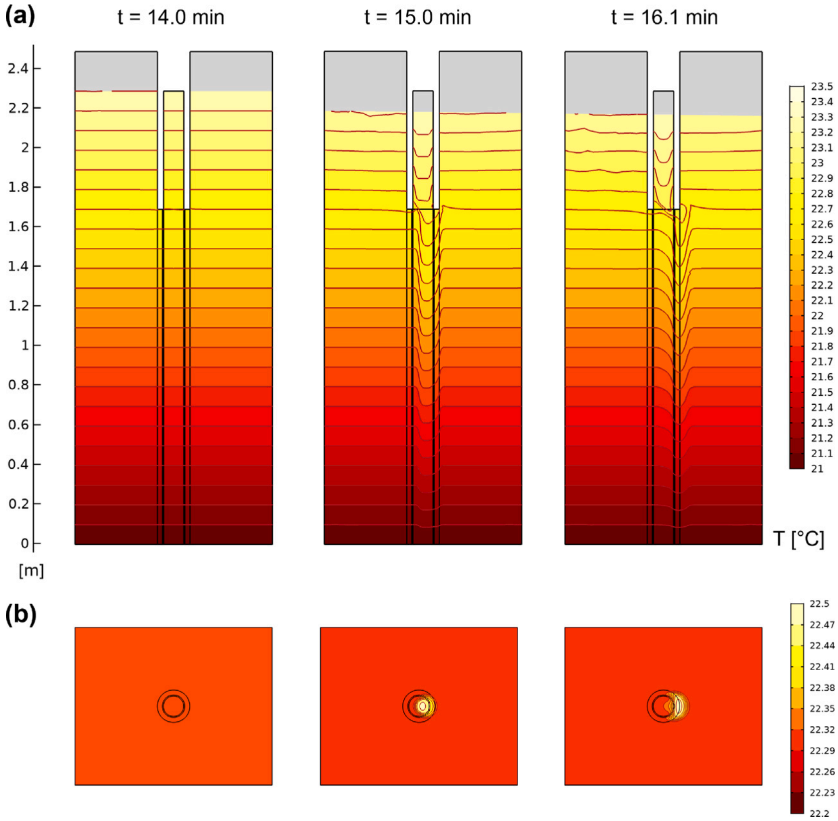

Fig. 5. (a) Temperature field [°C] on a 3D model cross section along an x-z plane passing through the center of the well, at three different time steps. (b) Temperature field [°C] on a 3D model cross sections along an x-y plane at 1.3 m from the bottom of the domain, at the corresponding time steps.

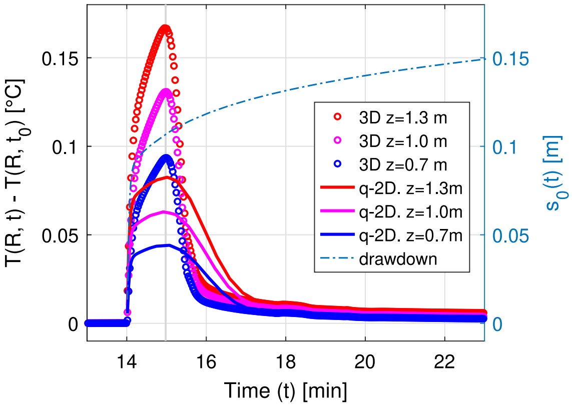

Fig. 6. Temperature anomaly simulated at the center of the well open space at three different depths as result of the 3D numerical model (dots), and as reproduced by the quasi-2D model (solid lines). The drawdown (dashed-dotted line) is referred to the right vertical axis.

are 0.033 °C at $z = 1.3$ m, 0.025 °C at $z = 1.0$ m, and 0.018 °C at $z = 0.7$ m. By a full inspection of the results of the 3D model, considering that the initial temperature vertical gradient is 1 °C/m, and the drawdown at the time of the peak approximately 0.1 m, this difference has to be attributed to the vertical components of the in-well velocity field being non homogeneous at given z, but rather showing a maximum close to the center of the borehole space and progressively reducing approaching the Γ interface, honoring the condition (6). On the other hand, the model proposed in Section 2.3, assumes a vertical plug flow motion. Despite this, capturing the timing of the peak allows us to obtain a fair estimate of the average horizontal velocities in the time interval $[t^\star - t_0]$.

3.2. Results of the sensitivity analysis

3.2.1. Sensitivity analysis on the steady flow field

Fig. 7(a) shows a comparison between the flow distortion factor α_D, as computed from the results of the 2D numerical model described in Section 2.4.1, and the one calculated using Eq. (A.2) proposed by Drost et al. (1968), for each parameter realization. The comparison shows a substantial agreement between the two, which lends support to the conceptualization and parameterization of the 2D numerical model. Slight deviations from the 1:1 line may be attributed to numerical errors of the model, particularly at very low in-well velocities (corresponding to the highest values of α_D).

In Fig. 7(b) the flow distortion factor α_D is plotted against the distortion factor $\alpha_S = u_0/q_\infty$ (Sano, 1983), where u_0 is the x component (parallel to $\boldsymbol{q}_\infty$) of the velocity at the center of the circular hole (i.e. $\mathbf{u}(0,0) = (u_0, 0)$). Both were computed from the results of the 2D model. The relationship between the two follows the 2/3 slope line, as the average velocity used to compute α_D, defined by (A.1), is approximately equal to 2/3 of the maximum velocity occurring at the center of the well open space, the profile $u(R, y)$ being approximately parabolic (Bayer-Raich et al., 2019).

Fig. 7(c) shows the relationship between the average velocity U_0^y and the average velocity U_0^x, defined according to (A.1) and (10), respectively, which is found to be well approximated by a line of slope 3/4.

The sensitivity indices relative to the distortion factor α_D are reported in Table 2, where only the permeabilities are considered as parameters.

The ensemble mean, variance, and skewness, of the distribution of α_D, both unconditional and conditional on the model parameters k_1, k_2 and k_3, are shown in Fig. 8. These parameters have been normalized

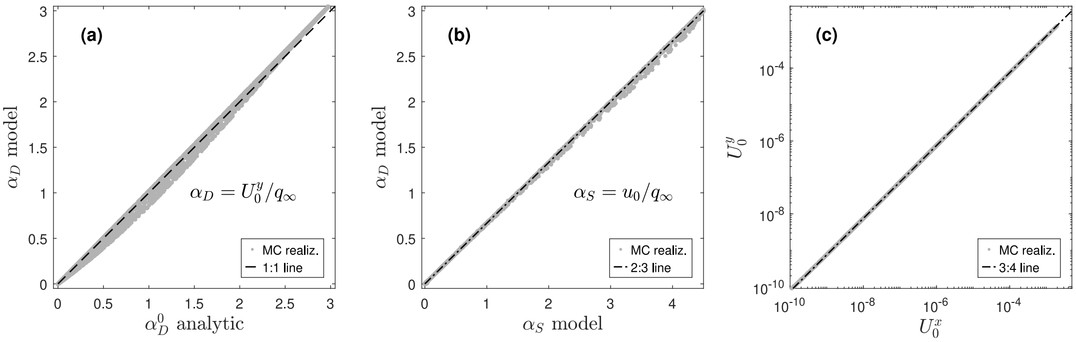

Fig. 7. (a) Comparison between the flow converge factor α_D as computed by using the analytic expression by Drost et al. (1968) and the one resulting from the 2D horizontal numerical model, for all the Monte Carlo realizations. (b) Comparison between the flow converge factors α_D and α_S by the numerical model. (c) Comparison between the average velocity U_0^x, defined by (10), and the average velocity U_0^y, defined by (A.1).

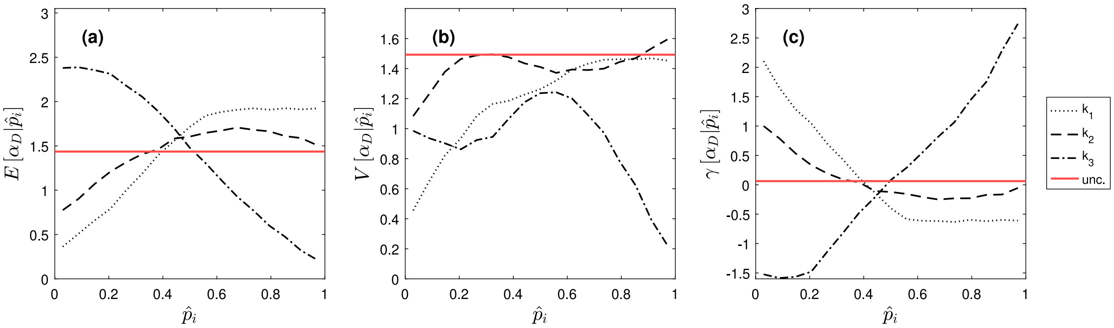

Fig. 8. Ensemble mean (a), variance (b) and skewness (c) of the flow distortion factor α_D, conditional to the dimensionless parameters $\hat{p}_i$. The red line indicates the unconditional corresponding statistical moment.

Table 2
Sensitivity indices for the flow distortion factor α_D.

α_D	k_1	k_2	k_3
$AMAE_i$	0.34	0.16	0.48
$AMAV_i$	0.20	0.06	0.39
S_i	0.20	0.05	0.39
$AMA\gamma_i$	12.2	4.64	18.6

according to

$$\hat{p}_i = \frac{p_i - p_i^{min}}{p_i^{max} - p_i^{min}} \tag{28}$$

where p_i^{max} and p_i^{min} are the maximum and minimum values, respectively, of the range of each parameter reported in Table 1.

These results show that the expected value of the flow distortion factor is less sensitive to the permeability of the filter pack k_2 and more sensitive to the permeability of the natural porous medium k_3. The latter has the major influence also on the variance and on the skewness of the final distribution of α_D. As visible in Fig. 8, low values of k_3 correspond to higher mean values of α_D, as already found analytically by Drost et al. (1968) and Sano (1983). Low values of k_1 correspond to lower values of α_D, similarly to what found by Bayer-Raich et al. (2019) on the well screen porosity. The variance conditional to k_3 or k_1 is always lower than the unconditional variance, as confirmed by the same values of $AMAV_i$ and principal Sobol's indexes S_i for these two parameters (see Table 2). Moreover, the influence of the well screen permeability k_1 on the expected value, the variance, and the skewness of α_D becomes negligible once a sufficiently large value is reached (Fig. 8).

In general, it can be observed that the uncertainty in the values of k_1, k_2 and k_3, gives rise to a considerable degree of uncertainty in determining the flow distortion factor α_D. Therefore, despite the ability of the methodology described above to estimate in-well water average velocities, a relevant degree of uncertainty persists in the estimation of the undisturbed Darcy's flow rate q_∞ from the latter, when permeabilities of the well screen, the filter pack and the natural porous medium are unknown. Naturally, this can be extended to any other in-well technique.

3.2.2. Sensitivity analysis on the temperature field

According to (22), Figs. 9(a–c) display the time required to recover 70% of the initial temperature perturbation in the 2D horizontal numerical model, indicated as t_{70}, at the center of the borehole space, as a function of U_0^x (10). The same plots show the curve described by Eq. (C.2) imposing $\beta = 0.7$. Fig. 9(c) shows the ensemble mean and the coefficient of variation of the average velocity U_0^x as functions of the recovery time t_{70}. Note that also in this case we use the average velocity defined by (10), rather than the one used to compute the convergence factor (A.1).

From Fig. 9 we can observe that the relationship between the t_{70} and the average in-well water velocity U_0^x, despite thermal parameters uncertainty, is essentially bijective for velocities larger than approximately 10^{-5} m/s (corresponding to $Pe_t \simeq 3.7$). In this velocity range, the numerical results show very good agreement with Eq. (C.1). For very large in-well water velocities, corresponding to t_{70} approximately lower than 10^0 minutes, the results of the 2D horizontal model display a very slight deviation from the curve (C.1), visible in Fig. 9(b). This is likely due to numerical instability of the 2D horizontal model arising at the largest velocities. Mesh refinement to control this numerical instability (through the Péclet's number of the elements) would have led to an increase in the computational time that would have precluded the execution of a large number of Monte Carlo realizations.

For velocities lower than approximately 10^{-5} m/s, even at thermal Péclet numbers larger than one, we observe a loss of bijection which is progressively exacerbated at $Pe_t < 1$ (here corresponding to $U_0^x <$

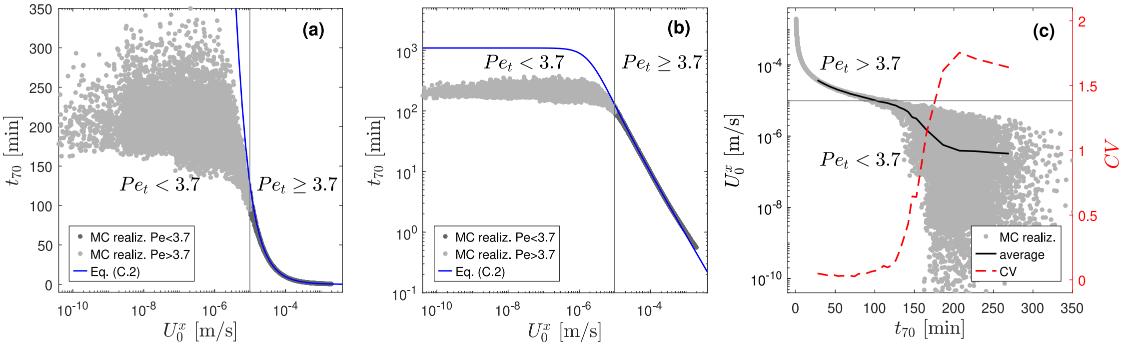

Fig. 9. (a) Time required to recover 70% of the temperature perturbation ($\beta = 0.7$) as a function of the (log) average in-well velocity along the x axis. The 1D analytic model (Eq. (C.2)) is displayed with a blue line. (b) The same as (a) but time is in log scale. (c) Ensemble mean (black) and coefficient of variation (red) of the average velocity U_0^x as a function of the recovery time t_{70}. The Monte Carlo realizations are displayed with a different color depending on the thermal Péclet number (18) in (a) and (b).

Table 3
Sensitivity indices for the recovery time t_{70}.

	k_1	k_2	k_3	ϕ_1	ϕ_2	ϕ_3	ρ_1	ρ_2	ρ_3	C_{p1}	C_{p2}	C_{p3}	λ_1	λ_2	λ_3
AMAE$_i$	0.08	0.13	0.24	0.02	0.02	0.02	0.01	0.03	0.01	0.01	0.02	0.01	0.03	0.08	0.04
AMAV$_i$	0.37	0.57	0.59	0.07	0.07	0.06	0.07	0.07	0.06	0.06	0.06	0.05	0.09	0.22	0.14
S$_i$	0.05	0.13	0.41	0.00	0.00	0.00	0.01	0.00	0.00	0.00	0.00	0.00	0.01	0.08	0.02

$2.7 \cdot 10^{-6}$ m/s). Likely, for $Pe_t < 3.7$, the variability in the thermal parameters of the well screen, the filter pack, and the natural porous medium begins to have an observable influence. Correspondingly, the coefficient of variation in Fig. 9(c) increases above 0.1. The coefficient of variation demonstrates that an estimate of the in-well velocity in the conduction-dominated regime, yet possible, would be subject to a high level of uncertainty if the material parameters of the different compartments are unknown. Moreover, in this region, the analytic model of Appendix C deviates from the numerical results, which supports the conclusion that this uncertainty has to be attributed to the influence of the well screen, the filter pack and the natural porous medium, that the 1D analytic model does not account for. In particular, in this regime, Eq. (C.2) gives rise to larger recovery times (Fig. 9(b)) due to the lower thermal diffusivity of water, on average, compared to the thermal diffusivities of the other material compartments. These results, capturing the transition between a thermal regime governed by advection and a thermal regime governed by conduction, also support a good selection of the parameter ranges (Table 1) for the scope of this analysis.

The sensitivity indices for the recovery time t_{70} are reported in Table 3. The ensemble mean and the ensemble variance of the distributions of recovery time t_{70}, conditional to the dimensionless model parameters $\hat{p}_i$, are shown in Fig. 10. All parameters have been made dimensionless according to (28).

From Fig. 10(a) it can be observed that the mean value of t_{70} is very sensitive to the permeability of the natural porous medium k_3. For large values of the latter (i.e. larger undisturbed Darcy's fluxes, the hydraulic gradient being fixed), the average recovery time is smaller, while it increases for the lowest values of k_3. The expected value is less sensitive to changes in the permeabilities of the well screen, k_1, and the filter pack, k_2. This is related to the fact that the permeabilities of the material compartments around the borehole space control the in-well velocity field, hence the role of advective heat transfer with respect to thermal conduction. A significant effect is exerted also by the thermal conductivity of the filter pack λ_2, particularly at its smallest values, as visible in Fig. 10(c). Little or negligible sensitivity of the expectation of t_{70} appears with respect to the other parameters. These observations are confirmed by the $AMAE_i$ indices reported in Table 3.

The variance of t_{70} appears to be mostly sensitive to the permeabilities, particularly k_2 and k_3, but a significant influence is also exerted by the thermal conductivities, particularly of the filter pack λ_2 and the natural porous medium λ_3. For both the expected value and the variance of t_{70}, the permeability of the natural porous medium k_3 appears to lose its influence when in the lower half of its parameter space ($\hat{p}_i < 0.5$), likely because these values of k_3 induce a conduction-dominated regime. A similar behavior is observed for lower values of k_2.

Overall, the results of the global sensitivity analysis on the t_{70} indicate that the thermal dissipation of a temperature anomaly in the well open space is mostly controlled by the permeabilities of the well screen, the gravel pack and, more significantly, of the porous medium, as these are the factors controlling the in-well horizontal flow field. Among the other parameters, the thermal conductivity of the filter pack appears to exert a significant influence, particularly at its lower values.

4. Discussion

Previous studies examined the effect of pumping activity on subsurface temperatures. Early research established a link between long-term changes in groundwater temperatures and groundwater abstraction (Taniguchi, 1995; Abe et al., 2014). Klepikova et al. (2025) showed that prolonged pumping alters the natural vertical temperature profile in both fractured and granular aquifers. Bense et al. (2020) used such profiles to quantify increased groundwater vertical fluxes associated with intensified aquifer exploitation. However, in contrast to the present study, these works focus on depths where the geothermal gradient dominates and on long temporal scales, ranging from years to decades.

At shorter time scales (hours to days), the analysis of temperature profiles under pumped conditions has been widely used to characterize the geometric and hydraulic properties of fractured aquifers (Klepikova et al., 2011; Chatelier et al., 2011; Klepikova et al., 2014; Pouladi et al., 2021). In unconsolidated formations, pumping is often combined with artificially induced temperature anomalies during active thermal tracer tests to enhance the advective component of heat transport (Klepikova et al., 2016; del Val et al., 2021). However, active thermal tracer tests require considerable experimental effort, limiting their applicability for long-term monitoring (Simon et al., 2022). Instead, the method proposed here does not require additional experimental endeavors beyond the deployment of downhole pressure and temperature measurement devices that are commonly used. Water velocities can be estimated via simple data post-processing, making the technique potentially suitable for long-term monitoring and data assimilation strategies, likely as a complement to tracer tests.

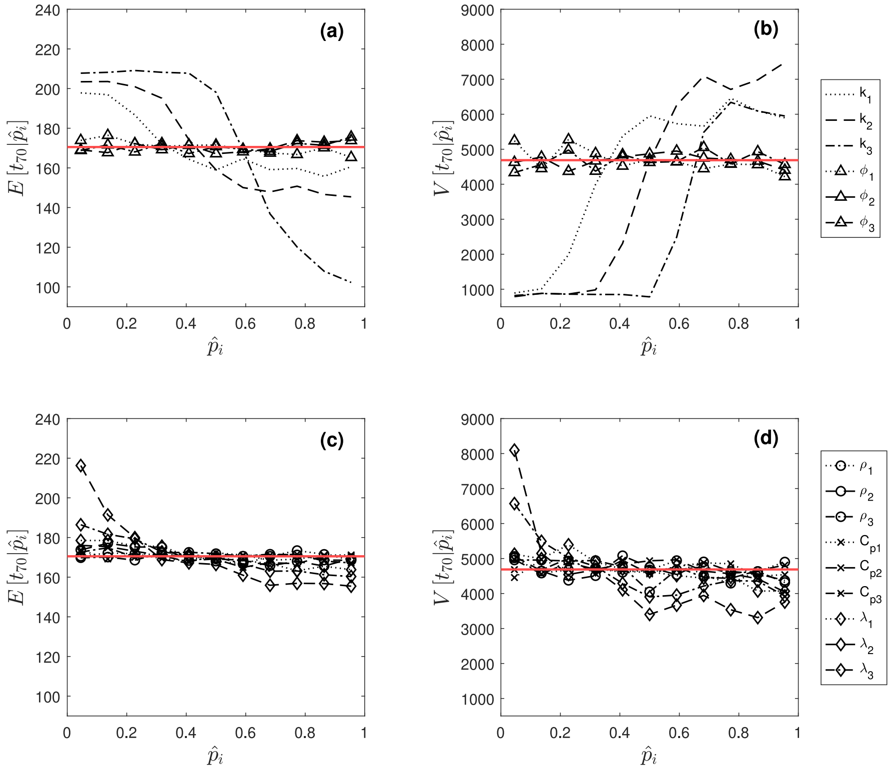

Fig. 10. Ensemble mean (a, c) and variance (b, d) of the recovery time t_{70}, conditional to the dimensionless parameters $\hat{p}$. The red line indicates the unconditional statistics.

In a sandy-gravelly aquifer, Patton et al. (2025) recently reported temperature fluctuations in observation boreholes at intermediate time scales (hours to days), driven by rapid groundwater level changes following heavy rainfall or increased river–aquifer exchanges. While the mechanism underlying the temperature perturbations analyzed by these authors appears similar to that of this study, hydraulic head variations in their case are driven by recharge events rather than by nearby pumping. In the present study, we unravel the temperature perturbations occurring in the zone of seasonal thermal regime of unconsolidated aquifers at short time scales (minutes to hours, depending on the horizontal velocities) in response to nearby intermittent pumping. This work thus contributes to demonstrating the potential of subsurface temperature time series to resolve groundwater flow processes across multiple temporal scales.

The short time scale of the process investigated in this study requires data collection at a high temporal resolution. An initial indication of the process time scale, related to site-specific horizontal groundwater flow rates, can be inferred from Fig. 9(b). Furthermore, experimental temperature data should be sufficiently accurate and precise, as temperature perturbations that can be observed under natural conditions are typically of the order of some decimals of °C. For effective application of the model proposed in Section 2.3, pressure head data should also be sufficiently accurate. In the experimental data presented in the Supplementary Information, for instance, pumping-induced temperature perturbations are well-captured and modeled using data from sensors with resolutions of 0.01 °C for temperature and 0.001 m for pressure head.

We speculate here that, to apply the presented method, experimental temperature measurements should be collected in a flow field that has not been significantly distorted by the presence of the measurement device during the drawdown or the recovery. However, a description of a suitable experimental setup goes beyond the scope of this paper and would require further investigation. Since temperature profiles in the seasonally dynamic thermal zone may exhibit variability and heterogeneities, such as due to preferential flow (Furlanetto et al., 2024) or variable recharge rates (Irvine et al., 2016), preliminary site-specific investigations are recommended. For example, deploying sensors at multiple depths could help delineate the zone in which these pumping-induced temperature perturbations are detectable.

5. Conclusions

In very shallow unconfined sedimentary aquifers with a naturally established and season-related vertical temperature gradient, when an observation well responds to the activation and deactivation of a nearby pumping well, its in-well temperature may exhibit a perturbation related to the vertical velocities in the water column. Concurrently, due to lateral heat transfer, this perturbation is progressively dissipated up to a new thermal equilibrium condition. These temperature perturbations may have implications when analyzing temperature data collected in monitoring wells. If these are employed, for instance, in the calibration/validation of groundwater models, they should be appropriately filtered, as these perturbations represent a consequence of the measurement setup that groundwater flow models will not be able to reproduce.

In the present study, we provided a mechanistic description of this phenomenon and validated it via 3D numerical modeling. Moreover, we proposed a quasi-2D semi-analytical model allowing us to model these perturbations and to estimate the average in-well horizontal velocity, provided that horizontal heat transport is not significantly influenced by the thermal parameters of the well screen, filter pack and the natural porous medium.

We conducted a global sensitivity analysis by means of Monte Carlo 2D (horizontal) numerical simulations. This allowed us to demonstrate that, when the dissipation of an initially homogeneous temperature anomaly in the well open space is advection-dominated, namely at thermal Peclet number approximately ≥ 3.7, the time required for its dissipation can be almost unambiguously linked to the in-well horizontal water velocity. Thus, the latter can be estimated with a fair degree of accuracy even under uncertainty on the thermal parameters of the system. At thermal Péclet numbers approximately < 3.7, when conductive heat transfer begins to compete with advection, in-well velocities cannot be determined unequivocally using thermal dissipation tests if the thermal parameters of the system are uncertain.

Future research should focus on laboratory and field experiments, aiming at validating the proposed models, likely comparing in-well water velocity estimates obtained through the methodology proposed here with direct measurements or estimates obtained through more traditional and well-established approaches. In addition, further investigations should focus on clarifying the influence of buoyancy-related free convection and the influence of instruments placed within the open space of the well on both the velocity and the temperature fields.

We conclude that, when measuring temperatures at shallow depths within monitoring wells responding to nearby pumping wells, it is important to monitor and analyze these pumping-induced temperature perturbations, as they represent a result of the field setup. At the same time, they can be a simple and informative tool for estimating in-well horizontal water velocities, especially if heat transfer is dominated by advection in the system under investigation.

Declaration of Generative AI and AI-assisted technologies in the writing process

During the preparation of this work, the author used ChatGPT and Writefull to improve the readability and language of the manuscript. The author reviewed and edited the content as needed and takes full responsibility for the content of the publication.

Declaration of competing interest

The authors declare that they have no known competing financial interests or personal relationships that could have appeared to influence the work reported in this paper.

Acknowledgments

The author would like to thank Matteo Camporese (University of Padova) for his valuable suggestions, and Leonardo Costa and Gianmarco Boscolo for the engaging and stimulating discussions. The author also thanks the anonymous reviewers for their constructive comments, which helped improve the quality of the manuscript.

Appendix A. Drost et al.'s distortion factor

Under the assumption of laminar flow, Drost et al. (1968) found that the average in-well velocity (Bayer-Raich et al., 2019)

$$\bar{u} = U_0^y = \frac{1}{2R}\int_{-R}^{R} u(0,y)\,dy \tag{A.1}$$

can be expressed as $\bar{u} = \alpha_D q_\infty$, where q_∞ is the undisturbed Darcy flow rate and α_D is a flow distortion factor given by the equation in Box I, where $R[L]$ is the inner radius of the well screen, $r_2[L]$ is the outer radius of the well screen, $r_3[L]$ is the outer radius of the filter pack (see Fig. 3(b)), and k_1, k_2 and k_3 are the permeabilities ($[L^2]$) of the well screen, the filter pack and the natural porous medium, respectively.

Appendix B. Derivation of Eq. (11)

Let us consider a cylindrical control volume that coincides with the portion of in-well water column along the screened interval of the observation well. This cylinder has a radius R $[L]$ and a height H [L]. We also assume that the vertical coordinate z is zero at the lower base of the control volume and positive upwards. Moreover, we assume a plug flow motion inside the well, so that the vertical components of the velocity field $[L\tau^{-1}]$ are $w = w(z,t)$, and that $w(z = 0, t) = 0$.

During the drawdown, an inflowing volumetric flow rate $Q_{in}(t)$ $[L^3\tau^{-1}]$ will enter the control volume from its upper base, and since the vertical velocity $w(z = H, t) = ds_0(t)/dt$, as long as the water table does not intersect the screened portion of the well, we have

$$Q_{in}(t) = \pi R^2 \frac{ds_0(t)}{dt}$$

An outflow flow rate will leave the control volume through the lateral surface, and we define a specific outflow rate $\omega(t)$ $[L^3\tau^{-1}L^{-2}]$. We assume that for a homogeneous aquifer $\omega(t)$ is homogeneous along z, so that $Q_{out}(t) = 2\pi RH\omega(t)$. Hence, we can write the mass balance $Q_{in} = Q_{out}$ as

$$2\pi RH\omega(t) = \pi R^2 \frac{ds_0(t)}{dt}$$

from which

$$\omega(t) = \frac{R}{2H}\frac{ds_0(t)}{dt} \tag{B.1}$$

Applying a similar mass balance to a cylindrical control volume extending from $z = 0$ to an arbitrary elevation z, we have

$$2\pi Rz\omega(t) = \pi R^2 w(z,t)$$

and by using (B.1), we obtain

$$w(z,t) = -\frac{z}{H}\frac{ds_0(t)}{dt} \tag{B.2}$$

where the negative sign was added to indicate that $w(z,t)$ is directed downward when $ds_0(t)/dt > 0$.

Appendix C. 1D analytic thermal dissipation equation

We illustrate here a simplified one-dimensional analytic solution for the process modeled in the sensitivity analysis.

Let us consider the 1D advection-conduction partial differential equation for heat transfer (15) in the infinitely extended purely-fluid 1D domain $x \in (-\infty, \infty)$. The constant and homogeneous velocity U_0^x is hereafter renamed u for brevity and is directed towards the positive x direction. The latter equation is subject to the initial condition:

$$T(x,0) = T_0, \quad x \in (-\infty, 0) \cup (D, \infty)$$
$$T(x,0) = T_1, \quad x \in [0, D]$$

where $D = 2R$, and to the boundary conditions:

$$T(-\infty,t) = T(\infty,t) = T_0, \quad t > 0$$
$$\frac{\partial T}{\partial x}(\pm\infty,t) = 0, \quad t > 0$$

Thus, like in the 2D-horizontal numerical model used for the sensitivity analysis, an initially homogeneous temperature anomaly $(T_1 - T_0)$ in $[0, D]$ begins to be dissipated for $t > 0$ under steady flow conditions.

$$\alpha_D = \frac{8}{\left(1+\frac{k_3}{k_2}\right)\left[1+\left(\frac{R}{r_2}\right)^2+\frac{k_2}{k_1}\left(1-\left(\frac{R}{r_2}\right)^2\right)\right]+\left(1-\frac{k_3}{k_2}\right)\left[\left(\frac{R}{r_3}\right)^2+\left(\frac{r_2}{r_3}\right)^2\right]+\frac{k_2}{k_1}\left[\left(\frac{R}{r_3}\right)^2-\left(\frac{r_2}{r_3}\right)^2\right]} \tag{A.2}$$

Box I.

Leveraging on the linearity of (15), a solution to this boundary-value problem can be found by the superposition of a constant solution and an adaptation of the solution that can be found in Carslaw and Jaeger (1959), obtaining

$$\frac{T(x,t)-T_0}{T_1-T_0}=\frac{1}{2}\left[erf\left(\frac{x-ut}{2\sqrt{\alpha_w t}}\right)-erf\left(\frac{x-ut-D}{2\sqrt{\alpha_w t}}\right)\right] \tag{C.1}$$

where $erf()$ denotes the error function. Given (22) and by evaluating (C.1) in $x = R$ (i.e. the center of the borehole space), we obtain

$$1-\beta(R,t)=\frac{1}{2}\left[erf\left(\frac{R-ut}{2\sqrt{\alpha_w t}}\right)+erf\left(\frac{R+ut}{2\sqrt{\alpha_w t}}\right)\right] \tag{C.2}$$

which relates the dimensionless recovery of the temperature perturbation β (22), time t and the average water velocity u.

Appendix D. Supplementary data

Supplementary material related to this article can be found online at https://doi.org/10.1016/j.advwatres.2025.105072.

Data availability

Data will be made available on request.

References

Abe, H., Tang, C., Kondoh, A., 2014. Effect of urban aquifer exploitation on subsurface temperature and water quality. Groundwater 52 (S1), 186–194. http://dx.doi.org/10.1111/gwat.12154.

Anderson, M.P., 2005. Heat as a ground water tracer. Groundwater 43 (6), 951–968. http://dx.doi.org/10.1111/j.1745-6584.2005.00052.x.

Arbogast, T., Brunson, D.S., 2007. A computational method for approximating a Darcy–Stokes system governing a vuggy porous medium. Comput. Geosci. 11, 207–218. http://dx.doi.org/10.1007/s10596-007-9043-0.

Bakx, W., Bense, V.F., Karaoulis, M., Oude Essink, G.H.P., Bierkens, M.F.P., 2023. Measuring groundwater flow velocities near drinking water extraction wells in unconsolidated sediments. Water 15 (12), http://dx.doi.org/10.3390/w15122167.

Bayer-Raich, M., Credoz, A., Guimerà, J., Jordana, S., Sampietro, D., Font-Capó, J., Nief, N., Grossemy, M., 2019. Estimates of horizontal groundwater flow velocities in boreholes. Groundwater 57 (4), 525–533. http://dx.doi.org/10.1111/gwat.12820.

Bear, J., 1988. Dynamics of Fluids in Porous Media. Dover Science Books, Dover, New York.

Bear, J., Cheng, A.H.D., 2009. Modeling Groundwater Flow and Contaminant Transport. Springer Dordrecht, http://dx.doi.org/10.1007/978-1-4020-6682-5.

Bense, V.F., Kooi, H., 2004. Temporal and spatial variations of shallow subsurface temperature as a record of lateral variations in groundwater flow. J. Geophys. Res.: Solid Earth 109 (B4), http://dx.doi.org/10.1029/2003JB002782.

Bense, V.F., Kurylyk, B.L., de Bruin, J.G.H., Visser, P., 2020. Repeated subsurface thermal profiling to reveal temporal variability in deep groundwater flow conditions. Water Resour. Res. 56 (6), http://dx.doi.org/10.1029/2019WR026913, e2019WR026913.

Bense, V.F., Read, T., Bour, O., Le Borgne, T., Coleman, T., Krause, S., Chalari, A., Mondanos, M., Ciocca, F., Selker, J.S., 2016. Distributed temperature sensing as a downhole tool in hydrogeology. Water Resour. Res. 52 (12), 9259–9273. http://dx.doi.org/10.1002/2016WR018869.

Bianchi Janetti, E., Guadagnini, L., Riva, M., Guadagnini, A., 2019. Global sensitivity analyses of multiple conceptual models with uncertain parameters driving groundwater flow in a regional-scale sedimentary aquifer. J. Hydrol. 574, 544–556. http://dx.doi.org/10.1016/j.jhydrol.2019.04.035.

Bravo, H.R., Jiang, F., Hunt, R.J., 2002. Using groundwater temperature data to constrain parameter estimation in a groundwater flow model of a wetland system. Water Resour. Res. 38 (8), 28–1–28–14. http://dx.doi.org/10.1029/2000WR000172.

Carslaw, H.S., Jaeger, J.C., 1959. Conduction of Heat in Solids, second ed. Oxford University Press.

Chatelier, M., Ruelleu, S., Bour, O., Porel, G., Delay, F., 2011. Combined fluid temperature and flow logging for the characterization of hydraulic structure in a fractured karst aquifer. J. Hydrol. 400 (3), 377–386. http://dx.doi.org/10.1016/j.jhydrol.2011.01.051.

Chen, K., Guo, Z., Yin, M., Liang, X., Chang, Z., Yang, S., Wei, X., Zhai, X., Zheng, C., 2024. Using rainfall-induced groundwater temperature response to estimate lateral flow velocity. Water Resour. Res. 60 (11), http://dx.doi.org/10.1029/2023WR036715, e2023WR036715.

COMSOL Multiphysics® v. 5.2, 2016. COMSOL AB. Stockholm, Sweden. https://www.comsol.com.

Constantz, J., 2008. Heat as a tracer to determine streambed water exchanges. Water Resour. Res. 44 (4), http://dx.doi.org/10.1029/2008WR006996.

de Marsily, G., 1986. Quantitative Hydrogeology: Groundwater Hydrology for Engineers. Academic Press, Orlando, Florida.

Dell'Oca, A., Riva, M., Guadagnini, A., 2017. Moment-based metrics for global sensitivity analysis of hydrological systems. Hydrol. Earth Syst. Sci. 21 (12), 6219–6234. http://dx.doi.org/10.5194/hess-21-6219-2017.

Devlin, J., 2020. Groundwater Velocity. The Groundwater Project, http://dx.doi.org/10.21083/978-1-77470-000-6.

Drost, W., Klotz, D., Koch, A., Moser, H., Neumaier, F., Rauert, W., 1968. Point dilution methods of investigating ground water flow by means of radioisotopes. Water Resour. Res. 4 (1), 125–146. http://dx.doi.org/10.1029/WR004i001p00125.

Furlanetto, D., Camporese, M., Schenato, L., Costa, L., Salandin, P., 2024. Fiber optics passive monitoring of groundwater temperature reveals three-dimensional structures in heterogeneous aquifers. Sci. Rep. 14, http://dx.doi.org/10.1038/s41598-024-58954-3.

Holzbecher, E., 2005. Inversion of temperature time series from near-surface porous sediments. J. Geophys. Eng. 2 (4), 343–348. http://dx.doi.org/10.1088/1742-2132/2/4/S07.

Irvine, D.J., Cartwright, I., Post, V.E., Simmons, C.T., Banks, E.W., 2016. Uncertainties in vertical groundwater fluxes from 1-D steady state heat transport analyses caused by heterogeneity, multidimensional flow, and climate change. Water Resour. Res. 52 (2), 813–826. http://dx.doi.org/10.1002/2015WR017702.

Jones, I., 1973. Low Reynolds number flow past a porous spherical shell. In: Mathematical Proceedings of the Cambridge Philosophical Society, vol. 73, (1), Cambridge University Press, pp. 231–238. http://dx.doi.org/10.1017/S0305004100047642.

Kaviany, M., 1995. Principles of Heat Transfer in Porous Media, second ed. Mechanical engineering series, Springer, New York.

Kearl, P.M., 1997. Observations of particle movement in a monitoring well using the colloidal borescope. J. Hydrol. 200 (1), 323–344. http://dx.doi.org/10.1016/S0022-1694(97)00026-7.

Klammler, H., Hatfield, K., Annable, M.D., Agyei, E., Parker, B.L., Cherry, J.A., Rao, P.S.C., 2007. General analytical treatment of the flow field relevant to the interpretation of passive fluxmeter measurements. Water Resour. Res. 43 (4), http://dx.doi.org/10.1029/2005WR004718.

Klepikova, M., Bense, V., Le Borgne, T., Guihéneuf, N., Bour, O., 2025. Impact of groundwater extraction on subsurface thermal regimes. Environ. Res. Lett. 20 (5), 054048. http://dx.doi.org/10.1088/1748-9326/adc8bb.

Klepikova, M.V., Le Borgne, T., Bour, O., Davy, P., 2011. A methodology for using borehole temperature-depth profiles under ambient, single and cross-borehole pumping conditions to estimate fracture hydraulic properties. J. Hydrol. 407 (1), 145–152. http://dx.doi.org/10.1016/j.jhydrol.2011.07.018.

Klepikova, M.V., Le Borgne, T., Bour, O., Gallagher, K., Hochreutener, R., Lavenant, N., 2014. Passive temperature tomography experiments to characterize transmissivity and connectivity of preferential flow paths in fractured media. J. Hydrol. 512, 549–562. http://dx.doi.org/10.1016/j.jhydrol.2014.03.018.

Klepikova, M., Wildemeersch, S., Hermans, T., Jamin, P., Orban, P., Nguyen, F., Brouyère, S., Dassargues, A., 2016. Heat tracer test in an alluvial aquifer: Field experiment and inverse modelling. J. Hydrol. 540, 812–823. http://dx.doi.org/10.1016/j.jhydrol.2016.06.066.

Kurylyk, B.L., Irvine, D.J., Bense, V.F., 2019. Theory, tools, and multidisciplinary applications for tracing groundwater fluxes from temperature profiles. WIREs Water 6 (1), e1329. http://dx.doi.org/10.1002/wat2.1329.

Kurylyk, B.L., Macquarrie, K., Caissie, D., Mckenzie, J., 2015. Shallow groundwater thermal sensitivity to climate change and land cover disturbances: Derivation of analytical expressions and implications for stream temperature modeling. Hydrol. Earth Syst. Sci. 19, 2469–2489. http://dx.doi.org/10.5194/hess-19-2469-2015.

Leaf, A.T., Hart, D.J., Bahr, J.M., 2012. Active thermal tracer tests for improved hydrostratigraphic characterization. Groundwater 50 (5), 726–735. http://dx.doi.org/10.1111/j.1745-6584.2012.00913.x.

Luce, C.H., Tonina, D., Gariglio, F., Applebee, R., 2013. Solutions for the diurnally forced advection-diffusion equation to estimate bulk fluid velocity and diffusivity in streambeds from temperature time series. Water Resour. Res. 49 (1), 488–506. http://dx.doi.org/10.1029/2012WR012380.

Neuman, S.P., 1972. Theory of flow in unconfined aquifers considering delayed response of the water table. Water Resour. Res. 8 (4), 1031–1045. http://dx.doi.org/10.1029/WR008i004p01031.

Patton, A.M., Cleall, P.J., Cuthbert, M.O., 2025. Using groundwater temperature time-series to reveal subsurface thermal and hydraulic processes. Hydrogeol. J. 1–19. http://dx.doi.org/10.1007/s10040-025-02930-2.

Pouladi, B., Bour, O., Longuevergne, L., de La Bernardie, J., Simon, N., 2021. Modelling borehole flows from distributed temperature sensing data to monitor groundwater dynamics in fractured media. J. Hydrol. 598, 126450. http://dx.doi.org/10.1016/j.jhydrol.2021.126450.

Raja Sekhar, G.P., Sano, O., 2000. Viscous flow past a circular/spherical void in porous media - An application to measurement of the velocity of groundwater by the single boring method. J. Phys. Soc. Japan 69 (8), 2479–2484. http://dx.doi.org/10.1143/JPSJ.69.2479.

Rau, G.C., Andersen, M.S., McCallum, A.M., Roshan, H., Acworth, R.I., 2014. Heat as a tracer to quantify water flow in near-surface sediments. Earth-Sci. Rev. 129, 40–58. http://dx.doi.org/10.1016/j.earscirev.2013.10.015.

Read, T., Bour, O., Bense, V., Le Borgne, T., Goderniaux, P., Klepikova, M., Hochreutener, R., Lavenant, N., Boschero, V., 2013. Characterizing groundwater flow and heat transport in fractured rock using fiber-optic distributed temperature sensing. Geophys. Res. Lett. 40 (10), 2055–2059. http://dx.doi.org/10.1002/grl.50397.

Saar, M., 2011. Review: Geothermal heat as a tracer of large-scale groundwater flow and as a means to determine permeability fields. Hydrogeol. J. 19, 31–52. http://dx.doi.org/10.1007/s10040-010-0657-2.

Saltelli, A., Annoni, P., Azzini, I., Campolongo, F., Ratto, M., Tarantola, S., 2010. Variance based sensitivity analysis of model output. Design and estimator for the total sensitivity index. Comput. Phys. Comm. 181 (2), 259–270. http://dx.doi.org/10.1016/j.cpc.2009.09.018.

Sano, O., 1983. Viscous flow past a cylindrical hole bored inside a porous media. J. Jpn. Soc. Fluids 2 (3), 252–259. http://dx.doi.org/10.11426/nagare1982.2.252.

Selker, J.S., Thévenaz, L., Huwald, H., Mallet, A., Luxemburg, W., van de Giesen, N., Stejskal, M., Zeman, J., Westhoff, M., Parlange, M.B., 2006. Distributed fiber-optic temperature sensing for hydrologic systems. Water Resour. Res. 42 (12), http://dx.doi.org/10.1029/2006WR005326.

Simon, N., Bour, O., Faucheux, M., Lavenant, N., Le Lay, H., Fovet, O., Thomas, Z., Longuevergne, L., 2022. Combining passive and active distributed temperature sensing measurements to locate and quantify groundwater discharge variability into a headwater stream. Hydrol. Earth Syst. Sci. 26 (5), 1459–1479. http://dx.doi.org/10.5194/hess-26-1459-2022, URL: https://hess.copernicus.org/articles/26/1459/2022/.

Sobol', I.M., 2001. Global sensitivity indices for nonlinear mathematical models and their Monte Carlo estimates. Math. Comput. Simulation 55 (1), 271–280. http://dx.doi.org/10.1016/S0378-4754(00)00270-6.

Stallman, R.W., 1965. Steady one-dimensional fluid flow in a semi-infinite porous medium with sinusoidal surface temperature. J. Geophys. Res. (1896- 1977) 70 (12), 2821–2827. http://dx.doi.org/10.1029/JZ070i012p02821.

Stonestrom, D.A., Constantz, J., 2003. Heat as a Tool for Studying the Movement of Ground Water near Streams, vol. 1260, US Department of the Interior, US Geological Survey.

Su, G.W., Jasperse, J., Seymour, D., Constantz, J., 2004. Estimation of hydraulic conductivity in an alluvial system using temperatures. Groundwater 42 (6), 890–901. http://dx.doi.org/10.1111/j.1745-6584.2004.t01-7-.x.

Suzuki, S., 1960. Percolation measurements based on heat flow through soil with special reference to paddy fields. J. Geophys. Res. (1896- 1977) 65 (9), 2883–2885. http://dx.doi.org/10.1029/JZ065i009p02883.

Taniguchi, M., 1993. Evaluation of vertical groundwater fluxes and thermal properties of aquifers based on transient temperature-depth profiles. Water Resour. Res. 29 (7), 2021–2026. http://dx.doi.org/10.1029/93WR00541.

Taniguchi, M., 1995. Analysing the long term reduction in groundwater temperature due to pun pumping. Hydrol. Sci. J. 40 (3), 407–421. http://dx.doi.org/10.1080/02626669509491424.

del Val, L., Carrera, J., Pool, M., Martínez, L., Casanovas, C., Bour, O., Folch, A., 2021. Heat dissipation test with fiber-optic distributed temperature sensing to estimate groundwater flux. Water Resour. Res. 57 (3), http://dx.doi.org/10.1029/2020WR027228, e2020WR027228.

Van Genuchten, M.T., 1980. A closed-form equation for predicting the hydraulic conductivity of unsaturated soils. Soil Sci. Am. J. 44 (5), 892–898.

Verreydt, G., Bronders, J., Van Keer, I., Diels, L., Vanderauwera, P., 2015. Groundwater flow field distortion by monitoring wells and passive flux meters. Groundwater 53 (6), 933–942. http://dx.doi.org/10.1111/gwat.12290.

Waples, D., Waples, J., 2004. A review and evaluation of specific heat capacities of rocks, minerals, and subsurface fluids. Part 1: minerals and nonporous rocks. Nat. Resour. Res. 13, 97–122. http://dx.doi.org/10.1023/B:NARR.0000032647.41046.e7.

Xie, Y., Batlle-Aguilar, J., 2017. Limits of heat as a tracer to quantify transient lateral river-aquifer exchanges. Water Resour. Res. 53 (9), 7740–7755. http://dx.doi.org/10.1002/2017WR021120.